



Nonequilibrium electron and lattice dynamics of Sb_2Te_3 under pressureKai Zhang ¹, Jiafeng Xie,² Jin Yang,¹ Huachao Jiang,¹ Shile Zhang,³ Zhi Zeng,¹ Xiaojia Chen,⁴ Tianwu Wang,^{2,*} and Fuhai Su ^{1,†}¹Key Laboratory of Materials Physics, Institute of Solid State Physics, HFIPS, Chinese Academy of Sciences, Hefei 230031, China²GBA Branch of Aerospace Information Research Institute, Chinese Academy of Sciences, Guangzhou 510700, China³Anhui Key Laboratory of Condensed Matter Physics at Extreme Conditions, High Magnetic Field Laboratory, HFIPS, Chinese Academy of Sciences, Hefei, Anhui 230031, China⁴Center for High Pressure Science and Technology Advanced Research, Shanghai 201203, China

(Received 2 November 2021; accepted 25 April 2022; published 6 May 2022)

Combined measurements including Raman scattering and optical pump-probe spectroscopy (OPPS) are carried out to investigate the lattice and electron dynamics of Sb_2Te_3 under hydrostatic pressures. The pressure evolutions of nonequilibrium photocarrier dynamics, containing the hot electron relaxations and coherent acoustic phonons, have been accessed up to 30 GPa. With increasing pressure, the Raman vibrations and electron relaxations manifest anomalies around 3 GPa and 5 GPa, indicating the sudden changes of electron-phonon couplings across the electronic topological transition (ETT) and semiconductor-semimetal transition (SST). Especially, the OPPS reveals that the hot phonon bottleneck is effectively suppressed along with the onset of ETT, which is likely due to the abrupt increase in the density of state and the number of energy valley in conduction band, basing on the calculated electronic and lattice structures. Furthermore, a comprehensive phase diagram of Sb_2Te_3 composed with ETT, SST, as well as the additional three high-pressure structures and a mixture phase has been distinguished according to the pressure behavior of OPPS. Our paper not only develop understandings for the interactions between electron and lattice in Sb_2Te_3 , but also may provide a strategy to probe the electronic topological changes under pressure.

DOI: [10.1103/PhysRevB.105.195109](https://doi.org/10.1103/PhysRevB.105.195109)**I. INTRODUCTION**

Topological insulators, hosting both insulating gap in the bulk state and a robust metallic surface or edge state [1,2], have attracted intense attractions due to their application prospects in quantum information [3], optoelectronic [4,5], and thermoelectric devices [6–8]. Among them, the quasi-two dimension Sb_2Te_3 is a star material, which exhibit an orthorhombic structure with the space group of R-3m [9–11]. Pressure modulation provides a simple and clean route to continuously tune the lattice and electronic structure in materials [12]. Sb_2Te_3 undergoes several sequent phase transitions from the ambient rhombohedral α phase to the high pressure monoclinic β , γ phases, and the alloyed cubic δ phase at around 7.7, 14.5, and 25 GPa with the space groups of C2/m, C2/c, and Im-3m, respectively [10,11]. In addition, an electronic topological transition (ETT) occurs at around 3 GPa, which features with the U shape-like changes of the compressibility [11,13,14], the anomaly of electronic transport [15,16] as well as the abnormal varieties in Raman spectra [17]. The Dirac surface electronic state, protected by the time-reversal symmetry, can maintain until the phase transition from semiconducting to semimetallic state at around 9.0 GPa [15]. Interestingly, it has been found that the compressed

Sb_2Te_3 serve as the promising candidate for a topological superconductor, where the superconductivity coexists with the topological state under pressure about 4 GPa [16,18]. The investigations of electron-phonon interactions under pressure are essential to understand the pressure-induced phenomena including topological transition, thermoelectric properties, superconductivity, however, which present huge challenges both in experiments and theoretical calculations.

Time-resolved ultrafast optical spectroscopy is a powerful tool to access the native complex interactions among diverse excitation species, such as hot carriers, phonons, excitons, etc., by disentangling different decay processes of the nonequilibrium carriers in time domain [19–22]. As for Sb_2Te_3 , typical multiple electronic relaxation processes along with high-frequency oscillations and a slow wiggle arising from coherent phonon have been observed from the transient differential reflectivity spectra at ambient condition [23–27]. The time constant as well as the amplitude for the fast decay process increases with increasing temperature and pump fluence, which is in accord with the two-temperature model (TTM) [28–33], and can be used to extract the electron-phonon coupling constant and the anharmonic collisions among phonons [24–27]. Under higher fluence case, the fast time constant, in turn, starts to decline with fluence [18,24], and even the crystalline structure of the Sb_2Te_3 renormalizes [34,35]. To date, however, the nonequilibrium electron and lattice dynamics under pressure of Sb_2Te_3 , especially the understanding of the pressure evolutions of the electron-

* wangtw@aircas.ac.cn

† fhsu@issp.ac.cn

phonon coupling and coherent phonons, which are important parameters to explore the topological physics and the superconductivity, have not been addressed yet.

In this paper, we combine the Raman scattering and optical pump-probe spectroscopy (OPPS) with the high-pressure diamond anvil cell (DAC) technology to investigate the vibrational properties and ultrafast dynamics in the Sb_2Te_3 under pressure. The transition pressures of the electronic and crystal structures are examined, and a phase diagram is established. In combination with the first-principles calculations, a ETT and a phase transition from semiconductive to semimetallic state are evidenced by the pressure behavior of Raman vibrations and photocarrier dynamics. Meanwhile, we find that the ETT extremely suppress the phonon bottleneck effect. Our paper provides important understandings for the fundamental physical properties in topological insulator materials under pressure.

II. EXPERIMENTAL METHODS

The high quality Sb_2Te_3 crystal was purchased from the SixCarbon Technology. The carrier density with p type was estimated to be about $n = 8.5 \times 10^{17} \text{ cm}^{-3}$ using the Hall measurement (see Fig. S1 in the Supplemental Material [36]). A DAC with the culet of $300 \mu\text{m}$ was applied to obtain high pressure. The thin-platelet sample with size around $40 \times 40 \mu\text{m}$ and thickness of $5 \mu\text{m}$ was cleaved from a Sb_2Te_3 crystal, and then was loaded in DAC together with a ruby particle. The sample has fresh smooth surfaces. Silicon oil was employed for the pressure transmitting medium to create quasi-hydrostatic pressure conditions. The Raman scattering measurement was performed using a 532-nm laser beam with the average power less than 2 mW before a $\times 20$ objective lens. The back-scattering signal was collected by a Charge Coupled Device after dispersed by an 1800 g/mm grating (designed by Princeton Instruments). For OPPS measurement, a Ti: Sapphire femtosecond oscillator (Mira F900, Coherent) with pulse duration of 150 fs, central wavelength of 800 nm, and repetition rate of 76 MHz was employed to generate pump and probe beams [37]. The polarization of the pump and probe beams were adjusted to be orthogonal using a polarized beam splitter cube, and then focused on the sample surface inside DAC by a $\times 10$ objective lens. The pump spot is at least 5 times bigger than the probe spot. The reflected probe signal modulated by the pump beam was detected by a biased silicon photodetector and then processed by a RF lock-in amplifier. Both Raman scattering and optical pump-probe experiments were performed under room temperature.

III. RESULTS AND DISCUSSION

Raman spectra of the Sb_2Te_3 at different pressures are presented in Fig. 1(a). All the spectra have been subtracted by constant backgrounds and displaced vertically for clarification. Three peaks associated with the A_{1g}^1 , E_g^2 , and A_{1g}^2 modes can be observed in the ambient α -phase Sb_2Te_3 , and all those modes show obvious blueshift with increasing pressure. This is in good agreement with the reported result [17]. Above 8.9 GPa, the intensities of all these three modes significantly reduces accompanied by the emergence of several new Raman

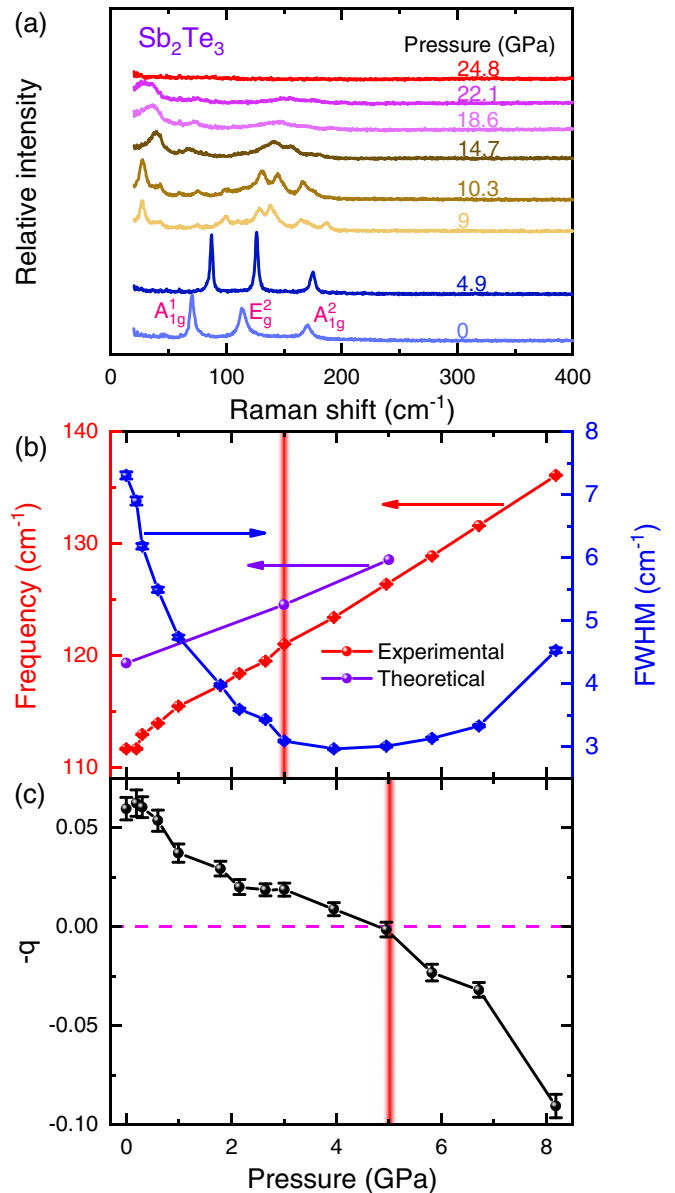


FIG. 1. (a) Raman spectra of the Sb_2Te_3 excited by a 532-nm laser at different pressures. [(b),(c)] Pressure dependencies of the frequency, FWHM, and Fano asymmetry parameter $-q$ of the Sb_2Te_3 fitted by Fano formula. The purple dots represent the calculated frequencies of E_g^2 -phonon mode at selected pressures

modes, which indicates the onset of the structural transition from the α phase to β phase [17]. The coexistence of the Raman modes both the α and β phases implies that the system enters into a mixed phase in the pressure range from 8.7 to 13 GPa. Those Raman modes of the α phase rapidly weaken in intensity as the pressure is increased. At around 18 GPa, all the observed Raman modes broaden and the peak at around 37 cm^{-1} exhibits a downshift with pressure, corresponding to the structural transition from the β phase to γ phase. Above the pressure of 23.3 GPa, all the Raman vibrational modes disappear instead of constant backgrounds. This signifies the entrance of the disorder δ phase, i.e., the high symmetry bcc phase with the space group of Im-3m . Interestingly, these

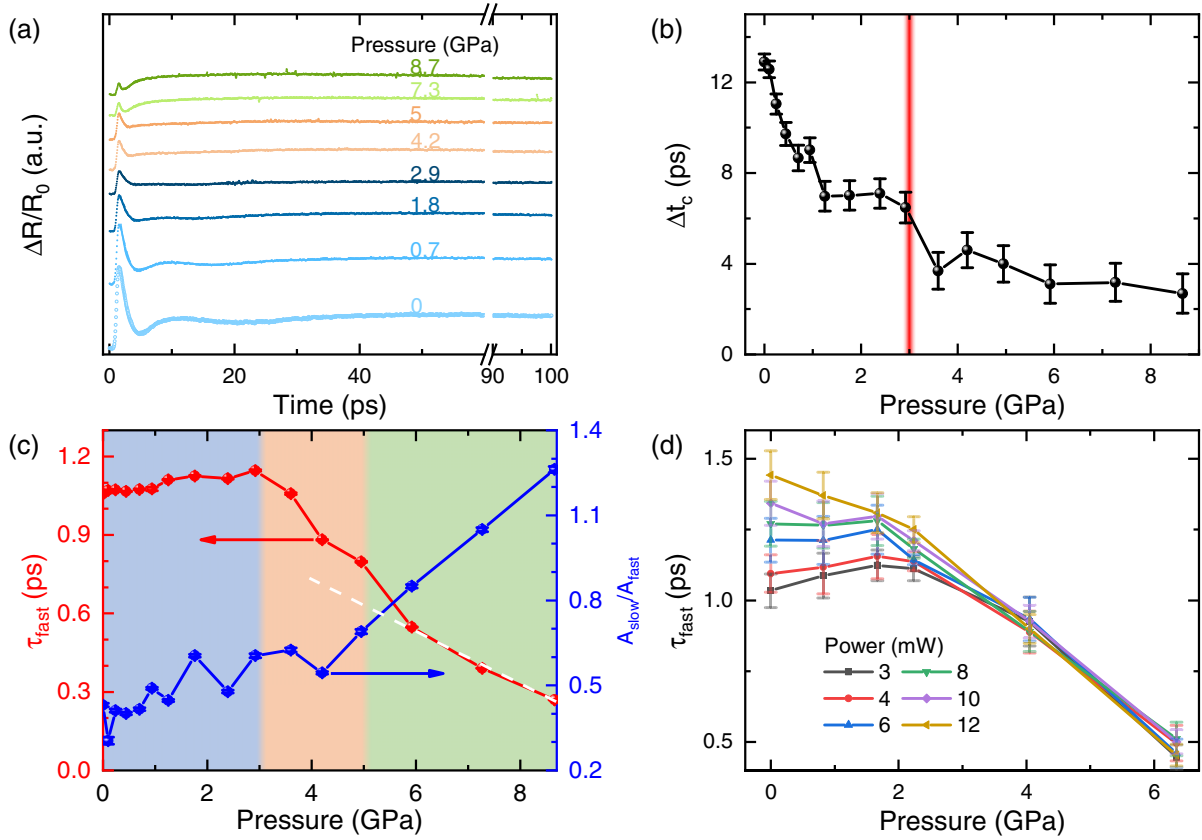


FIG. 2. (a) Transient differential reflectivity $\Delta R/R_0$ at different pressures. (b) Pressure dependence of the extracted characteristic time Δt_c of the coherent acoustic phonon adopts by the method shown in Fig. S2(a) in the Supplemental Material [36]. (c) Pressure dependence of the fast decay time τ_{fast} and the amplitude ratio $A_{\text{slow}}/A_{\text{fast}}$ of the slow and fast processes. Areas of the ETT and SST have been depicted by different colors. The dashed lines present the linear fits of the corresponding data. (d) Fast decay time τ_{fast} at different pump fluences and pressures.

three Raman modes in the first α phase show asymmetric line profiles dictated by the electron-lattice interactions. We fit the middle E_g^2 peak at around 110 cm^{-1} by a Fano formula [21,38–41],

$$I(\omega) = A \left[q + \frac{\omega - \omega_0}{\Gamma} \right]^2 / \left[1 + \left(\frac{\omega - \omega_0}{\Gamma} \right)^2 \right] + E \quad (1)$$

where $I(\omega)$ is the measured intensity, ω_0 , Γ , and A are the frequency, half width at half maximum, and intensity of the fitted peak, E is the background signal, q is the Fano asymmetry parameter. The fitted frequency and full width at half maximum (FWHM) (twice of the Γ) of the E_g^2 mode are shown in Fig. 1(b). Similar to the previous reports [17], the pressure coefficient of this modes decreases at around 3 GPa due to the occurrence of the ETT. The FWHM significantly reduces with pressure up to 3 GPa and then gradually increases under higher pressures. Figure 1(c) presents the extracted $-q$ value as the function of pressure. Broadening of the first-order Raman line toward the high (low) energy side is a “fingerprint” of the Fano-type interference from hole (electron)-type carriers, thereby the $-q$ value serves as an indicator of carrier type [41–43]. For the Raman Stokes-side spectra, $-q$ is positive at ambient pressure, which indicates that the dominant carrier of the as-grown Sb_2Te_3 single crystal in this experiment is hole-type, which is consistent with our Hall measurement (see

Fig. S1 in the Supplemental Material [36] for more details). With increasing pressure, the $-q$ monotonously declines and changes the sign from positive to negative at around 5 GPa. This implies that the carrier type becomes to electron-type. This result is in accord with the pressure behavior of Hall coefficient of Sb_2Te_3 reported by J. Zhu *et al.*, by which the dominated carrier was found to switch from hole- to electron-type at 7.2 GPa [16]. The discrepancy of the transition pressure may result from the different doping level of the as-grown samples by defects and/or impurities, which can influence the Fermi level to some extent [13,44,45]. The observed flip of the carrier type should be a signature of a change in electronic structure [16,46], which will be further verified by the following optical pump-probe experiment.

To further interrogate the electron-phonon (e-ph) interactions, the OPPS measurements under pressure were carried out. The time-domain differential reflectivity (DR) transients, i.e., $\Delta R/R_0 = (R - R_0)/R_0$, of Sb_2Te_3 at different pressures below 8.7 GPa are displayed in Fig. 2(a), where R and R_0 are the reflectivity with and without the pump excitation, respectively. Similar with previous papers [34], the DR signal at ambient condition shows an initial immediate increase upon photoexcitation, followed by a fast decay and a subsequent long-live offset supervised with a low frequency oscillation. The fast decay component corresponds to the energy relaxation of the photocarrier through optical phonon scattering,

while the oscillation is attributed to the coherent longitudinal acoustic phonon (LAP) [23–27]. It should be mentioned that we did not identify the high-frequency periodical oscillations arising from the coherent optical phonons under pressure due to the limitations in the duration and energy of laser pulse in our measurement [35]. The amplitude of the fast component of the DR transient is obviously reduced as increasing pressure. Meanwhile, the long-live component become gradually robust relative to the fast decay with increasing pressure, even dominating over the DR signal above 7 GPa. We fit the DR curve at each pressure by using a multiple-exponential function. At low-pressure range (0–3 GPa), the LAP signal can be reproduced using a term with damped harmonic oscillator combined with an exponential function. However, the oscillations are dramatically attenuated in amplitude and shortened in lifetime so that they cannot be simulated successfully, as shown in Figs. S2(a) and S2(b) in the Supplemental Material [36], presenting the more data and 2D color map under pressures. In order to evaluate the pressure evolution of the LAP frequencies, we simply take the time interval Δt_c between the wave peak and valley of oscillation as the half period of the coherent LAP [24]. The pressure dependence of the Δt_c is shown in Fig. 2(b), which shows a rapid decrement with increasing pressure, while the pace decreases above ~ 3 GPa. The coherent LAP in Sb_2Te_3 origins from the periodic modulation of the dielectric function along the c axis by pump beam, and the frequency f_{cap} is determined by the sound velocity v_s in term of the pulse propagation model [47], i.e., $f_{\text{cap}} = 2nv_s \cos(\theta)/\lambda_{\text{probe}}$. Here n is the refraction index of Sb_2Te_3 , v_s is the sound speed in Sb_2Te_3 , θ is the incident angle of the probe beam ($\sim 45^\circ$), and λ_{probe} is the probe wavelength (800 nm). The steady reflectivity of the Sb_2Te_3 moderately declines with increasing pressure (see Fig. S2c in the Supplemental Material [36]), this implies that the refraction index n at 800 nm also slightly decreases with pressure. Thus, the v_s should increase with increasing pressure. This is reasonable in view of the gradually decreasing distance along the c axis and the increasing interlayer interaction with pressure [11,13,14].

The fitted time constant of the fast decay component τ_{fast} is shown in Fig. 2(c) as a function of pressure. As can be seen that the τ_{fast} first increases moderately with increasing pressure until it reaches a maximum at around 3 GPa and starts to decline instead. This turning point is in line with that of the aforementioned pressure behavior of FWHM of Raman mode, signaling the occurrence of the ETT [17]. According to the two temperature model (TTM), the τ_{fast} is governed by the e-ph coupling strength, that is, $\tau_{\text{fast}} = \pi k_B T_e / 3\hbar\lambda\langle\omega^2\rangle$. Here the second moment $\lambda\langle\omega^2\rangle$ of the Eliashberg function describes the strength of the electron-phonon interaction [33]. Therefore, the anomaly of around 3 GPa likely indicate that the sudden change of e-ph coupling across the ETT, accompanying with the distinct increase of DOS as proven by the following energy-band structure calculations. Upon further compressing, the τ_{fast} shows a distinct drop at around 5 GPa. The discontinuous change of the τ_{fast} at around 5 GPa implies that a disturbance occurs on the electronic structure, and is suggested to be the SST as referring to the aforementioned Raman results.

In Fig. 2(c), we also display the pressure dependent ratio between the maximum amplitude for slow and fast processes,

defined as $A_{\text{slow}}/A_{\text{fast}}$. One can see that the $A_{\text{slow}}/A_{\text{fast}}$ augment with elevating pressure, even exceeding 1 above 7 GPa. It is noteworthy that the pressure dependence of $A_{\text{slow}}/A_{\text{fast}}$ exhibit a discontinuity around 3 GPa, that is, the increasing rate become larger at high-pressure range (4–8.7 GPa) than in the low-pressure region. As for semiconductor phase, the electron-hole pairs with excess kinetics energy are injected immediately via interband transition upon above-bandgap photoexcitation, which is followed by a rapid thermalization through electron-electron scattering within a few tens femtoseconds. Therefore, the quasi-Fermi-Dirac distributions for electrons with higher carrier temperature (T_e) than lattice (T_L) is created. The succeeding energy dissipations of hot carriers toward lattice through high-frequency optical phonons scatterings is encoded in the fast decay component. However, the high-frequency LO optical phonons participating in the carrier cooling tend to set a threshold for the energy relaxation, i.e., the optical phonon emission is expected to be inefficient as the energy of electron is lower than that of optical phonon [48]. Thereby, the subsequent energy relaxation is dominated by the e-ph scattering through low-frequency acoustic phonons, behave as a long decay in DR signal. In addition, the interband relaxations related with direct electron-hole recombination or surface defect assisted trapping should also be taken into account for the slow decay of DR transient in semiconductor phase.

On the other hand, the generated LO phonons normally decay into low-energy acoustic phonons through anharmonic interactions. However, if the decay rate is not enough fast and does not balance with the optical phonon emission during hot carriers cooling process, it may result in the temporal accumulation of LO phonons in population and form the hot phonon distribution with high temperature approaching T_e . Such hot phonons act as a heat bath and reheat the carriers by optical phonon reabsorption, which manifests the hot phonon bottleneck (HPB), retarding the photocarrier relaxation [49,50]. Since the HPB effect generally enhance with increasing photocarrier density or carrier temperature, we performed high-pressure OPPS measurements under different pump fluence in order to examine how the pressure influence the HBP. As shown in Fig. S4 in the Supplemental Material [36], illustrating the normalized DR transients for different pump fluences at 0–6 GPa, the fast decay process slows down obviously with increasing pressure below 4 GPa, while varies negligibly under high pressure range. The obtained pressure dependent fast time constants τ_{fast} at each fluence are shown in Fig. 2(d). We can see that the τ_{fast} is prolonged with increasing pump level under ambient condition, emphasizing the existence of HPB in Sb_2Te_3 . With increasing pressure, the pump-fluence dependence become weaker, indeed, the τ_{fast} is not sensitive to the pump power above 4 GPa. It indicates that the HPB effect is reduced with pressure, and disappears together with the ETT under high pressure. In general, different factors associated with the phonon structures, including the phononic density of states (DOS), phonon gap, and up-conversion of acoustic phonon, impact the HPB [24,26,51]. Thus, to clarify the pressure effect on the HPB, we calculated the phonon structures of Sb_2Te_3 at 0, 3, and 5 GPa basing on the first-principles calculations [52–57], shown in Fig. S3 in the Supplemental Material [36]. The pressure

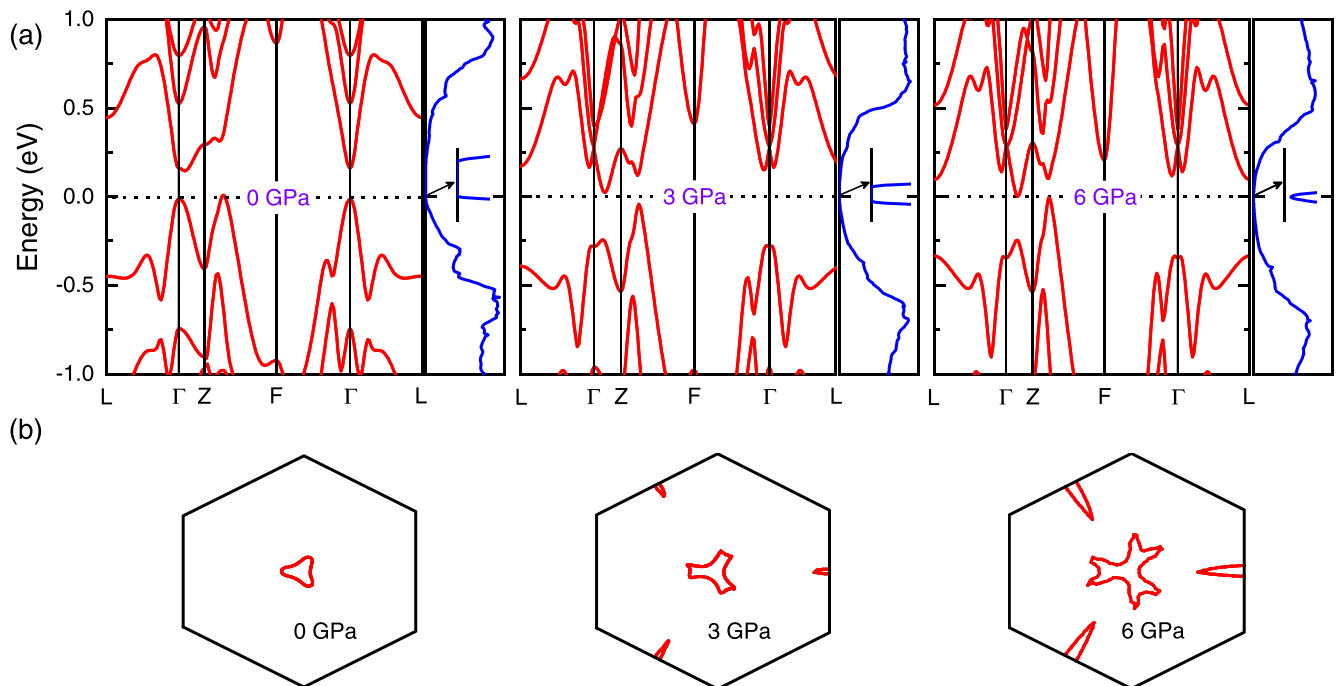


FIG. 3. (a) Band structures and the density of state for the bulk state of the Sb_2Te_3 at 0, 3, and 6 GPa with considering the spin-orbit coupling. The dashed lines donate the zero energy levels, which locate at the bottom of the conduction bands. Insets are the enlarged description of the DOS near the zero energy level. (b) Constant-energy sections with the electronic energy of 0.2 eV under different pressures.

dependence of the calculated frequency of E_g^2 mode is shown in Fig. 1(b), which approaches the experimental result. First, the calculations reveal that the phonon DOS decreases with increasing pressure. Such reduction in DOS should help to block the decay of high-frequency optical phonon toward the low-frequency branches, which would enhance the HPB. This is sharply in contrast with our observation. Second, the opening (closing) of the phonon band gap between the optical and acoustical branches can slow down (speed up) the carrier cooling and strengthen (suppress) the HPB effect. However, we do not see obvious changes in phonon gaps with pressure. In addition, the up-conversions from acoustic phonons to LO phonons may give rise to the HPB in Sb_2Te_3 . However, it is expected that such up-conversion should be more robust with increasing pressure considering the enhanced interlayer interactions and anharmonic scattering rate with increasing pressure [58]. All in all, from the calculated phonon structures, we find that the complete suppression of the HPB cannot be explained by the continuous variety of lattice structure with pressure. The sudden changes in electronic structures should be taken into account.

Herein, we speculate that the pressure dependence of HBP has a close correlation with the ETT because the HPB starts to undergo the significant suppression as the ETT take place. We simulate the electronic structures and calculate the density of the state (DOS) for the bulk state of the Sb_2Te_3 at 0, 3, and 6 GPa basing on the DFT, shown in Fig. 3(a). Here, we neglect the topological insulating surface state because that the Raman scattering and optical pump-probe spectroscopies is insensitive to the surface state for the bulk materials [59]. At ambient condition, Sb_2Te_3 exhibits a typical insulating state with a narrow band gap. With increasing pressure, the

conduction band gradually shifts down and the valence band moves up except that at the F- Γ -L direction. Above 3 GPa, the DOS increases pronouncedly and the G valley splits into multiple pockets, highlighting the occurrence of ETT. With further compression, the conduction and valence bands overlap above 6 GPa, indicating the formation of semimetallic state, which agree well with the aforementioned pressure behavior of Raman and DR spectra. First of all, the increase of DOS and the formation of multiple energy valleys around the bottom of conduction band can render more available phase space at low-energy range, allowing for more state occupations at lower energy side. As a result, the initial carrier temperature is decreased as long as the quasi-Fermi-Dirac distribution build up over a few tens femtoseconds upon photoexcitation. Such inverse relations between carrier temperature and DOS have been witnessed in other materials such as graphene [60]. In fact, our experimental results shown in Fig. 2(c), where the weight of the fast decay component obviously reduces with increasing pressure, can also attest the relative decrease in carrier temperature. The fast decay component corresponds to the optical phonon scattering, requiring the participations of high-energy electrons. Hence, the decrease of the weight of the fast decay component indicates that the ratio of hot electrons distributed over high-energy side reduces. Consequently, the population of hot phonons emitted from the relatively “cold” carriers, due to the DOS increases across ETT, is expected to decrease, which help to weaken the HPB.

Second, the changes of the topology of constant energy surface with pressure also influence the HPB. As the ETT occurs above the pressure of 3 GPa, the emergence of multiple energy valleys in the conduction band is able to increase the number of the k-space pathway toward low-energy sides for the

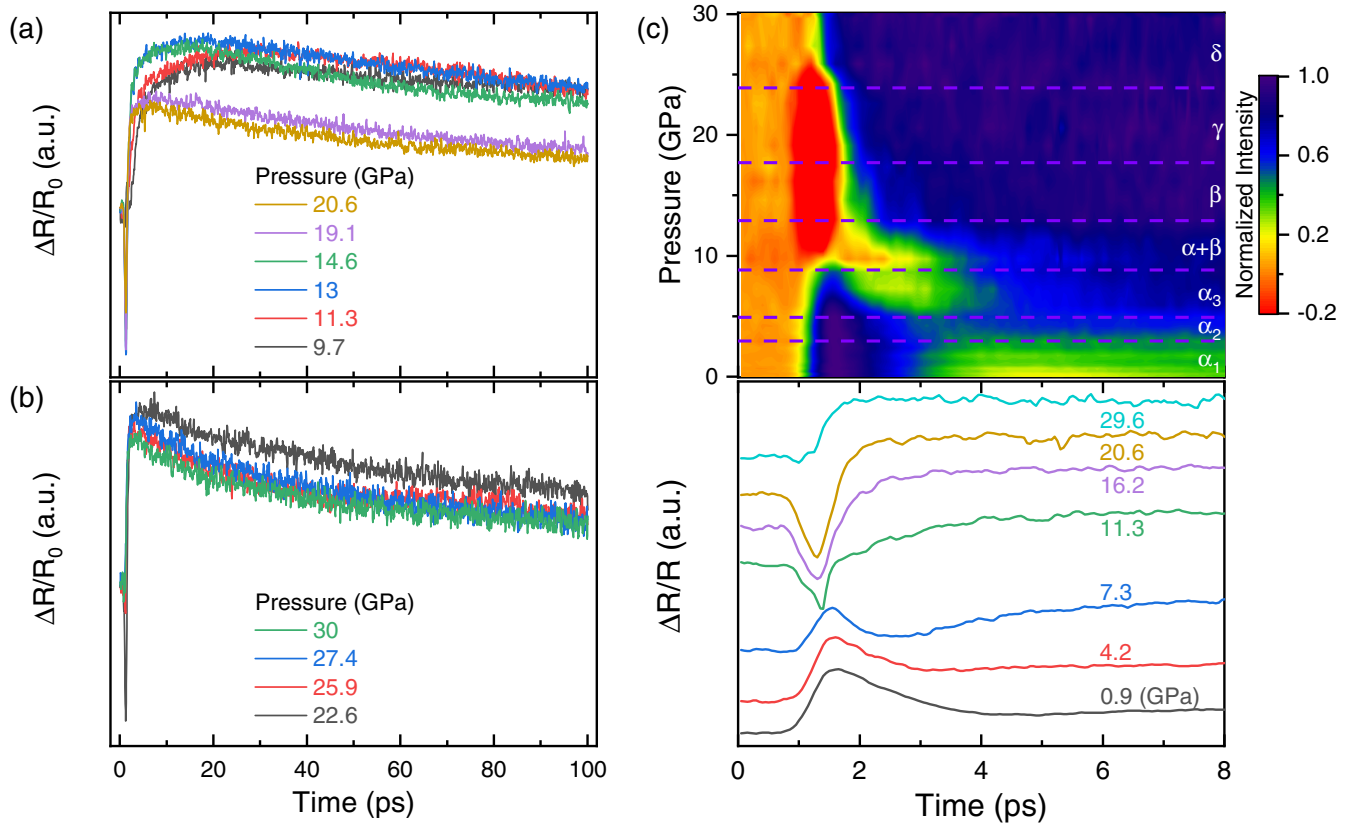


FIG. 4. [(a),(b)] Transient differential reflectivity $\Delta R/R_0$ of Sb_2Te_3 at different pressures. (c) Intensity map of the DR signal for the initial 8 ps of the Sb_2Te_3 . Spectra at several typical pressures are presented for clarification. Each phase has been marked by vertical-dashed lines and labeled above the map. $\alpha+\beta$ means the mixture phase containing both the α and β phases.

photocarrier relaxations. Accordingly, the emitted phonons from hot carriers have larger momentum ranges at high pressures. Such an extension in phonon distribution is beneficial to relieve the phonon accumulation effect in limited q space, and help to speed up the decay toward the acoustic phonons by relaxing the restrictions of momentum conservation [31]. Consequently, the phonon temperature reduces and the HPB effect is suppressed.

In the next, we proceed to investigate the pressure evolutions of photocarrier dynamics resulting from the lattice structural transitions at higher pressure range. Figures 4(a) and 4(b) present the transient DR signals of Sb_2Te_3 under pressure ranging from 9.7 to 20.6 GPa. Obviously, the $\Delta R/R_0$ is dramatically changed compared with that in low-pressure range shown in Fig. 2(a): Above 9 GPa, the DR transient start to show an initial rapid drop, followed by a fast rise within 2 ps and a slow intermediate increasing stage during 2–20 ps time range, as well as a subsequent slow decay lasting for a few hundred picoseconds. Such pressure behavior should be attributed to the structural phase transition from α phase to β phase. The intermediate stage become shorter and disappear when the pressure is higher than 18 GPa (see Fig. S5 in the Supplemental Material [36] for more details), in line with the turning pressure for the structure change from the pure monoclinic sevenfold β phase to the eightfold γ phase [10,11]. Furthermore, the photocarrier dynamics within initial time window of 8 ps in the whole studied pressure range are summarized in the Fig. 4(c) as the color map, where the DR

signals are normalized in amplitude for clarity. The different phase transitions can be distinguished more clearly from the contour plot. (i) For α phase below 8.9 GPa, it is divided into three regions with 0–3.0 GPa, 3.0–5.0 GPa, 5.0–8.9 GPa, defined as α_1 phase, α_2 phase, and α_3 phase, respectively, basing on the anomalies of DR signals. As discussed above, the onset of ETT at 3.0 GPa brings out the abrupt decrease of the time constant and amplitude weight for the fast decay component, further SST above 5 GPa leads to an additional drop following with a rise after 2 ps. (ii) Above 9 GPa, the sign of DR signal around 1.3 ps is switched from positive to negative, and an additional rising process (1.3–3.0 ps) can be disentangled, nevertheless, is totally dampened beyond 13 GPa. This pressure behavior indicates that the α and β phases likely coexist in the region of 9–13 GPa. (iii) With increasing pressure, the fast drop (or negative dip) of the DR signal around 1.3 ps rapidly vanishes above 23 GPa, marking the occurrence of disorder δ phase.

As we can see, the pressure evolution of photocarrier dynamics unveils a complete high-pressure phase diagram of the Sb_2Te_3 up to 30 GPa. The photoexcitation with femtosecond laser pulses is able to inject the nonequilibrium hot carriers far away the band extremes or Fermi surfaces, simultaneously, launch the intertwining between high-energy electrons and high-frequency optical phonons. Thereby, the ultrafast optical spectra are expected to be more sensitive to the pressure-induced varieties of dispersions of electronic (phonon) structures, especially at high k (q) ranges, than the

measurements obtained by steady spectroscopies including optical absorption, Raman, as well as electronic transport methods [37]. Although the scenarios and mechanism of photocarrier dynamics for β , γ , and δ phase of Sb_2Te_3 under high pressure region are not clear yet, these experimental results demonstrate the feasibility to diagnose the phase transitions from the electronic topologies and lattices structures under pressure by the ultrafast spectroscopies.

IV. CONCLUSIONS

In conclusion, a combined investigation on the lattice vibrations and ultrafast photocarrier dynamics of Sb_2Te_3 crystal in the pressure range from 0 to 30 GPa has been carried out using Raman scattering and ultrafast OPPS. The frequency and FWHM of the Raman modes exhibit abnormal variations at around 3 GPa, and the Fano asymmetry parameter shows a sign flip at around 5 GPa, corresponding to the ETT and SST, respectively. Furthermore, the pressure evolution of time-domain DR transient, imprinting the e-ph coupling information on the relaxation process, also presents

the anomalies across ETT and SST. Intriguingly, the HPB effects are observed at low pressures, however, are completely suppressed as ETT take place, which can be attributed to the increase of DOS and the formation of multiple energy valleys in conduction band basing on the calculated electronic and lattice structures. With further increasing pressure, we find that the pressure dependence of DR traces exactly reflects the lattice structure transitions including α - β and β - γ phase changes, as well as the mixed phase. Our paper develops understandings for the e-ph interactions in Sb_2Te_3 , and also provide impetus to explore the ultrafast photocarrier dynamics across electronic topological changes under pressure.

ACKNOWLEDGMENTS

This work was supported by National Natural Science Foundation of China (Grants No. 12004387, No. 11774354, No. 12174398, No. 51727806, and No. 12127807), Science Challenge Project (No. TZ2016001), CAS Innovation Grant (No. CXJJ-19-B08), and Hefei Science Center CAS (Grant No. 2018HSCKPRD003).

-
- [1] Y. L. Chen, J. G. Analytis, J. H. Chu, Z. K. Liu, S. K. Mo, X. L. Qi, H. J. Zhang, D. H. Lu, X. Dai, Z. Fang *et al.*, Experimental realization of a three-dimensional topological insulator, Bi_2Te_3 , *Science* **325**, 178 (2009).
- [2] H. Zhang, C. X. Liu, X. L. Qi, X. Dai, Z. Fang, and S. C. Zhang, Topological insulators in Bi_2Se_3 , Bi_2Te_3 and Sb_2Te_3 with a single Dirac cone on the surface, *Nat. Phys.* **5**, 438 (2009).
- [3] C. Nayak, S. H. Simon, A. Stern, M. Freedman, and S. D. Sarma, Non-Abelian anyons and topological quantum computation, *Rev. Mod. Phys.* **80**, 1083 (2008).
- [4] M. Z. Hasan and C. L. Kane, Colloquium: Topological insulators, *Rev. Mod. Phys.* **82**, 3045 (2010).
- [5] J. E. Moore, The birth of topological insulators, *Nature (London)* **464**, 194 (2010).
- [6] R. Venkatasubramanian, E. Siivola, T. Colpitts, and B. O'quinn, Thin-film thermoelectric devices with high room-temperature figures of merit, *Nature (London)* **413**, 597 (2001).
- [7] P. Ghaemi, R. S. K. Mong, and J. E. Moore, In-Plane Transport and Enhanced Thermoelectric Performance in Thin Films of the Topological Insulators Bi_2Te_3 and Bi_2Se_3 , *Phys. Rev. Lett.* **105**, 166603 (2010).
- [8] N. F. Hinsche, B. Y. Yavorsky, I. Mertig, and P. Zahn, Influence of strain on anisotropic thermoelectric transport in Bi_2Te_3 and Sb_2Te_3 , *Phys. Rev. B* **84**, 165214 (2011).
- [9] N. Sakai, T. Kajiwara, K. Takemura, S. Minomura, and Y. Fujii, Pressure-induced phase transition in Sb_2Te_3 , *Solid State Commun.* **40**, 1045 (1981).
- [10] Y. Ma, G. Liu, P. Zhu, H. Wang, X. Wang, Q. Cui, J. Liu, and Y. Ma, Determinations of the high-pressure crystal structures of Sb_2Te_3 , *J. Phys.: Condens. Matter* **24**, 475403 (2012).
- [11] S. M. Souza, C. M. Poffffo, D. M. Trichês, J. C. De Lima, T. A. Grandi, A. Polian, and M. Gauthier, High pressure monoclinic phases of Sb_2Te_3 , *Phys. B: Condens. Matter* **407**, 3781 (2012).
- [12] H.-K. Mao, X.-J. Chen, Y. Ding, B. Li, and L. Wang, Solids, liquids, and gases under high pressure, *Rev. Mod. Phys.* **90**, 015007 (2018).
- [13] K. Zhao, Y. Wang, Y. Sui, C. Xin, X. Wang, Y. Wang, Z. Liu, and B. Li, First principles study of isostructural phase transition in Sb_2Te_3 under high pressure, *Phys. Status Solidi RRL* **9**, 379 (2015).
- [14] A. Gaul, Q. Peng, D. J. Singh, G. Ramanath, and T. Borca-Tasciuc, Pressure-induced insulator-to-metal transitions for enhancing thermoelectric power factor in bismuth telluride-based alloys, *Phys. Chem. Chem. Phys.* **19**, 12784 (2017).
- [15] J. Zhang, T. Hu, J. Yan, F. Ke, J. Wang, X. Cui, X. Li, Y. Ma, J. Yang, and C. Gao, Pressure driven semi-metallic phase transition of Sb_2Te_3 , *Mater. Lett.* **209**, 78 (2017).
- [16] J. Zhu, J. L. Zhang, P. P. Kong, S. J. Zhang, X. H. Yu, J. L. Zhu, Q. Q. Liu, X. Li, R. C. Yu, R. Ahuja *et al.*, Superconductivity in topological insulator Sb_2Te_3 induced by pressure, *Sci. Rep.* **3**, 2016 (2013).
- [17] O. Gomis, R. Vilaplana, F. Manjón, P. Rodríguez-Hernández, E. Pérez-González, A. Muñoz, V. Kucek, and C. Drasar, Lattice dynamics of Sb_2Te_3 at high pressures, *Phys. Rev. B* **84**, 174305 (2011).
- [18] J. L. Zhang, S. J. Zhang, H. M. Weng, W. Zhang, L. X. Yang, Q. Q. Liu, S. M. Feng, X. C. Wang, R. C. Yu, L. Z. Cao *et al.*, Pressure-induced superconductivity in topological parent compound Bi_2Te_3 , *Proc. Natl. Acad. Sci. USA* **108**, 24 (2011).
- [19] T. Lin, L. Shi, Z. Wang, S. Zhang, Q. Liu, T. Hu, T. Dong, D. Wu, and N. Wang, Optical spectroscopy and ultrafast pump-probe study on $\text{Bi}_2\text{Rh}_3\text{Se}_2$: Evidence for charge density wave order formation, *Phys. Rev. B* **101**, 205112 (2020).
- [20] Y. Liu, Y. Zhang, J. Dong, H. Lee, Z. Wei, W. Zhang, C. Chen, H. Yuan, Y.-F. Yang, and J. Qi, Hybridization Dynamics in CeCoIn_5 Revealed by Ultrafast Optical Spectroscopy, *Phys. Rev. Lett.* **124**, 057404 (2020).
- [21] R. Mondal, A. Arai, Y. Saito, P. Fons, A. V. Kolobov, J. Tominaga, and M. Hase, Coherent Dirac plasmons in topological insulators, *Phys. Rev. B* **97**, 144306 (2018).
- [22] M. Zhang, Z. Wang, Y. Li, L. Shi, D. Wu, T. Lin, S. Zhang, Y. Liu, Q. Liu, J. Wang, T. Dong, and N. L. Wang, Light-Induced

- Subpicosecond Lattice Symmetry Switch in MoTe₂, *Phys. Rev. X* **9**, 021036 (2019).
- [23] H. J. Zeiger, J. Vidal, T. K. Cheng, E. P. Ippen, G. Dresselhaus, and M. S. Dresselhaus, Theory for dispersive excitation of coherent phonons, *Phys. Rev. B* **45**, 768 (1992).
- [24] N. Kumar, B. A. Ruzicka, N. P. Butch, P. Syers, K. Kirshenbaum, J. Paglione, and H. Zhao, Spatially resolved femtosecond pump-probe study of topological insulator Bi₂Se₃, *Phys. Rev. B* **83**, 235306 (2011).
- [25] Y.-P. Lai, H.-J. Chen, K.-H. Wu, and J.-M. Liu, Temperature-dependent carrier-phonon coupling in topological insulator Bi₂Se₃, *Appl. Phys. Lett.* **105**, 232110 (2014).
- [26] L. Cheng, C. La-o Vorakiat, C. S. Tang, S. K. Nair, B. Xia, L. Wang, J.-X. Zhu, and E. E. M. Chia, Temperature-dependent ultrafast carrier and phonon dynamics of topological insulator Bi_{1.5}Sb_{0.5}Te_{1.8}Se_{1.2}, *Appl. Phys. Lett.* **104**, 211906 (2014).
- [27] H.-J. Chen, K.-H. Wu, C.-W. Luo, T. Uen, J.-Y. Juang, J.-Y. Lin, T. Kobayashi, H.-D. Yang, R. Sankar, F. C. Chou *et al.*, Phonon dynamics in Cu_xBi₂Se₃ (x=0, 0.1, 0.125) and Bi₂Se₂ crystals studied using femtosecond spectroscopy, *Appl. Phys. Lett.* **101**, 121912 (2012).
- [28] S. D. Brorson, A. Kazeroonian, J. S. Moodera, D. W. Face, T. K. Cheng, E. P. Ippen, M. S. Dresselhaus, and G. Dresselhaus, Femtosecond Room-Temperature Measurement of the Electron-Phonon Coupling Constant γ in Metallic Superconductors, *Phys. Rev. Lett.* **64**, 2172 (1990).
- [29] M. I. Kaganov, I. M. Lifshitz, and L. V. Tanatarov, Relaxation between electrons and the crystalline lattice, *Zh. Eksp. Teor. Fiz.* **31**, 232 (1956) [*Sov. Phys. JETP* **4**, 173 (1957)].
- [30] V. V. Kabanov and A. S. Alexandrov, Electron relaxation in metals: Theory and exact analytical solutions, *Phys. Rev. B* **78**, 174514 (2008).
- [31] D. König, K. Casalenuovo, Y. Takeda, G. Conibeer, J. F. Guillemoles, R. Patteron, L. M. Huang, and M. A. Green, Hot carrier solar cells: Principles, materials and design, *Phys. E* **42**, 2862 (2010).
- [32] S. I. Anisimov, B. L. Kapeliovich, T. L. Perelman, Electron emission from metal surfaces exposed to ultrashort laser pulses, *Sov. Phys. -JETP* **39**, 375 (1974).
- [33] P. B. Allen, Theory of Thermal Relaxation of Electrons in Metals, *Phys. Rev. Lett.* **59**, 1460 (1987).
- [34] Y. Li, V. A. Stoica, L. Endicott, G. Wang, C. Uher, and R. Clarke, Coherent optical phonon spectroscopy studies of femtosecond-laser modified Sb₂Te₃ films, *Appl. Phys. Lett.* **97**, 171908 (2010).
- [35] S. Li, H. Huang, W. Zhu, W. Wang, K. Chen, D.-X. Yao, Y. Wang, T. Lai, Y. Wu, and F. Gan, Femtosecond laser induced crystallization of amorphous Sb₂Te₃ film and coherent phonon spectroscopy characterization and optical injection of electron spins, *J. Appl. Phys.* **110**, 053523 (2011).
- [36] See Supplemental Material at <http://link.aps.org/supplemental/10.1103/PhysRevB.105.195109> for additional information about the materials and methods.
- [37] K. Zhang, H. Jiang, J. Yang, J. Zhang, Z. Zeng, X. Chen, and F. Su, Pressure effects on the lattice vibrations and ultrafast photocarrier dynamics in 2H-TaS₂, *Appl. Phys. Lett.* **117**, 101105 (2020).
- [38] B. Friedl, C. Thomsen, and M. Cardona, Determination of the Superconducting Gap in RBa₂Cu₃O_{7- δ} , *Phys. Rev. Lett.* **65**, 915 (1990).
- [39] J. Bäckström, M. Rübhausen, M. Käll, L. Börjesson, A. P. Litvinchuk, M. Kakihana, M. Osada, and B. Dabrowski, Raman scattering in YBa₂Cu₄O₈ and PrBa₂Cu₄O₈: Indications of pseudogap effects in nonsuperconducting PrBa₂Cu₄O₈, *Phys. Rev. B* **61**, 7049 (2000).
- [40] E. Altendorf, X. K. Chen, J. C. Irwin, R. Liang, and W. N. Hardy, Temperature dependencies of the 340-, 440-, and 500-cm⁻¹ Raman modes of YBa₂Cu₃O_y for 6.7 \leq y \leq 7.0, *Phys. Rev. B* **47**, 8140 (1993).
- [41] V. Magidson and R. Beserman, Fano-type interference in the Raman spectrum of photoexcited Si, *Phys. Rev. B* **66**, 195206 (2002).
- [42] F. Cerdeira, T. A. Fjeldly, and M. Cardona, Effect of free carriers on zone-center vibrational modes in heavily doped *p*-type Si. II. Optical modes, *Phys. Rev. B* **8**, 4734 (1973).
- [43] M. Balkanski, K. P. Jain, R. Beserman, and M. Jouanne, Theory of interference distortion of Raman scattering line shapes in semiconductors, *Phys. Rev. B* **12**, 4328 (1975).
- [44] F. J. Manjón, R. Vilaplana, O. Gomis, E. Pérez-González, D. Santamaría-Pérez, V. Marín-Borrás, A. Segura, J. González, P. Rodríguez-Hernández, A. Muñoz *et al.*, High pressure studies of topological insulators Bi₂Se₃, Bi₂Te₃, and Sb₂Te₃, *Phys. Status Solidi B* **250**, 669 (2013).
- [45] Y. Jiang, Y. Y. Sun, M. Chen, Y. Wang, Z. Li, C. Song, K. He, L. Wang, X. Chen, Q.-K. Xue, X. Ma, and S. B. Zhang, Fermi-Level Tuning of Epitaxial Sb₂Te₃ Thin Films on Graphene by Regulating Intrinsic Defects and Substrate Transfer Doping, *Phys. Rev. Lett.* **108**, 066809 (2012).
- [46] J. Guo, H. Wang, F. Von Rohr, W. Yi, Y. Zhou, Z. Wang, S. Cai, S. Zhang, X. Li, Y. Li, J. Liu, K. Yang, A. Li, S. Jiang, Q. Wu, T. Xiang, R. J. Cava, and L. Sun, Electron-hole balance and the anomalous pressure-dependent superconductivity in black phosphorus, *Phys. Rev. B* **96**, 224513 (2017).
- [47] C. Thomsen, H. T. Grahn, H. J. Maris, and J. Tauc, Surface generation and detection of phonons by picosecond light pulses, *Phys. Rev. B* **34**, 4129 (1986).
- [48] A. Othonos, Probing ultrafast carrier and phonon dynamics in semiconductors, *J. Appl. Phys.* **83**, 1789 (1998).
- [49] H. Wang, J. H. Strait, P. A. George, S. Shivaraman, V. B. Shields, M. Chandrashekar, J. Hwang, F. Rana, M. G. Spencer, C. S. Ruiz-Vargas *et al.*, Ultrafast relaxation dynamics of hot optical phonons in graphene, *Appl. Phys. Lett.* **96**, 081917 (2010).
- [50] E. A. A. Pogna, X. Jia, A. Principi, A. Block, L. Banszerus, J. Zhang, X. Liu, T. Sohler, S. Forti, K. Soundarapandian *et al.*, Hot-carrier cooling in high-quality graphene is intrinsically limited by optical phonons, *ACS Nano* **15**, 11285 (2021).
- [51] J. Yang, X. Wen, H. Xia, R. Sheng, Q. Ma, J. Kim, P. Tapping, T. Harada, T. W. Kee, F. Huang *et al.*, Acoustic-optical phonon up-conversion and hot-phonon bottleneck in lead-halide perovskites, *Nat. Commun.* **8**, 14120 (2017).
- [52] P. E. Blöchl, Projector augmented-wave method, *Phys. Rev. B* **50**, 17953 (1994).
- [53] G. Kresse and J. Furthmüller, Efficiency of *ab-initio* total energy calculations for metals and semiconductors using a plane-wave basis set, *Comput. Mater. Sci.* **6**, 15 (1996).

- [54] J. P. Perdew, K. Burke, and M. Ernzerhof, Generalized Gradient Approximation Made Simple, *Phys. Rev. Lett.* **77**, 3865 (1996).
- [55] H. J. Monkhorst and J. D. Pack, Special points for Brillouin-zone integrations, *Phys. Rev. B* **13**, 5188 (1976).
- [56] V. Wang, N. Xu, J.-C. Liu, G. Tang, and W.-T. Geng, VASPKIT: A user-friendly interface facilitating high-throughput computing and analysis using VASP code, *Comput. Phys. Commun.* **267**, 108033 (2021).
- [57] A. Togo and I. Tanaka, First principles phonon calculations in materials science, *Scr. Mater.* **108**, 1 (2015).
- [58] X. Meng, T. Pandey, J. Jeong, S. Fu, J. Yang, K. Chen, A. Singh, F. He, X. Xu, J. Zhou, W.-P. Hsieh, A. K. Singh, J.-F. Lin, and Y. Wang, Thermal Conductivity Enhancement in MoS₂ under Extreme Strain, *Phys. Rev. Lett.* **122**, 155901 (2019).
- [59] R. Valdés Aguilar, J. Qi, M. Brahlek, N. Bansal, A. Azad, J. Bowlan, S. Oh, A. J. Taylor, R. P. Prasankumar, and D. A. Yarotski, Time-resolved terahertz dynamics in thin films of the topological insulator Bi₂Se₃, *Appl. Phys. Lett.* **106**, 011901 (2015).
- [60] W. K. Tse and S. D. Sarma, Energy relaxation of hot Dirac fermions in graphene, *Phys. Rev. B* **79**, 235406 (2009).